PHYSICAL REVIEW A **94**, 013423 (2016)

Relativistic calculations of angle-dependent photoemission time delay

Anatoli Kheifets[*]
Research School of Physics and Engineering, Australian National University, Canberra ACT 0200, Australia

Ankur Mandal[†] and Pranawa C. Deshmukh[‡]
Department of Physics, Indian Institute of Technology Madras, Chennai, Tamil Nadu 600036, India

Valeriy K. Dolmatov[§]
Department of Physics and Earth Science, University of North Alabama, Florence, Alabama 35632, USA

David A. Keating[‖] and Steven T. Manson[¶]
Department of Physics and Astronomy, Georgia State University, Atlanta, Georgia 30303, USA

(Received 20 May 2016; published 25 July 2016)

Angular dependence of photoemission time delay for the valence $np_{3/2}$ and $np_{1/2}$ subshells of Ar, Kr, and Xe is studied in the dipole relativistic random phase approximation. Strong angular anisotropy of the time delay is reproduced near respective Cooper minima while the spin-orbit splitting affects the time delay near threshold.

DOI: 10.1103/PhysRevA.94.013423

I. INTRODUCTION

A measurable time delay in laser-driven atomic ionization has been discovered recently [1,2]. Since the first pioneering experiments, the time-delay spectroscopy of laser-induced atomic ionization (attosecond chronoscopy) has become a rapidly developing field [3]. Among other characteristic features, an angular anisotropy of attosecond time delay relative to polarization of laser light has been predicted theoretically [4,5] and measured experimentally [6]. In single-photon ionization of atomic np subshells, the time delay can show some angular anisotropy due to the interplay of the ϵs and ϵd photoelectron continua [4,5]. This anisotropy becomes particularly strong near a Cooper minimum in the dominant $np \to \epsilon d$ channel, making the nominally weak $np \to \epsilon s$ channel competitive. In two-color (two-photon) XUV and IR experiments, the interference of these photoemission channels can manifest itself even in a spherically symmetric ns atomic subshell. This leads to a strong angular anisotropy of the measured time delay when the ϵd continuum has a kinematic node near the magic angle of 54.7°. Such a strong anisotropy has indeed been measured in He in a recent RABBITT (Reconstruction of Attosecond Beating By Interference of Two-photon Transitions) experiment [6]. Another interesting aspect of photoemission time delay is its sensitivity to the fine structure of the ionized target. Recent RABBITT experiments have detected such a sensitivity in the valence shell photoionization of the Kr and Xe atoms [7].

Atomic time delay measured in XUV/IR two-photon ionization experiments contains two distinct components:

$$\tau_a = \tau_W + \tau_{CLC}. \tag{1}$$

The so-called Wigner time delay τ_W is associated with the XUV photon absorption and can be related to the photoelectron group delay [8]. The second component τ_{CLC} is associated with the IR photon absorption and appears due to the coupling of the IR laser field and the Coulomb field of the ion remainder [the Coulomb-laser coupling (CLC) [9], also known as the continuum-continuum CC correction [10]].

In this paper, we concentrate primarily on the Wigner component of the atomic time delay and investigate its angular and spin dependence using the dipole relativistic random phase approximation (RRPA). We expand our previous relativistic studies of the Wigner time delay [11,12] and include the full interference of all the spin-orbit coupled photoionization channels. In the previous studies, only the time delay in the dominant channel was evaluated. We validate our theoretical model using the angular dependent time delay near the Cooper minimum of the $3p$ subshell of Ar. For the relatively light Ar atom, our RRPA results agree very well with nonrelativistic random-phase approximation with exchange (RPAE)[1] calculations [4]. For heavier Kr and Xe atoms, we clearly observe the manifestation of relativistic effects. One such effect is a spin-orbit splitting of the time delay near threshold.

We pay somewhat lesser attention to the CLC component of the time delay. This correction is known to decrease rapidly with a growing photoelectron energy. It is expected to be relatively small near the Cooper minimum, which is at least 30 eV or more above the threshold in the valence shells of noble gases. Hydrogenic estimates in Ref. [5] bound this correction to less than 20 as in this photoelectron energy range. Also, this correction is largely uniform across all the partial waves (see, e.g., Fig. 7 of Ref. [10]) and hence is not expected to be strongly angular dependent. However, this correction is very large near threshold, and it has to be taken into account near

---

[*] a.kheifets@anu.edu.au
[†] amankur@physics.iitm.ac.in
[‡] pcd@physics.iitm.ac.in
[§] vkdolmatov@una.edu
[‖] dkeating2@student.gsu.edu
[¶] smanson@gsu.edu

[1] The same exchange interaction is accounted for in both the RPAE and RRPA, but E is dropped from the latter acronym for brevity.

threshold. We do so by augmenting our RRPA results for τ_W with hydrogenic results from Ref. [5] for τ_{CLC}.

The paper is organized as follows. In Sec. II a a brief theoretical formulation is given. In Sec. III the results for the angle and energy dependence of Wigner time delay for photoemission from outer $np_{1/2}$ and $np_{3/2}$ subshells of atomic Ar, Kr, and Xe are presented and discussed; Ne is omitted because there is no Cooper minimum in its photoionization cross section. Conclusions are drawn in Sec. IV.

II. THEORETICAL METHOD

A. Photoionization amplitude

We adopt the multichannel RRPA formalism of Johnson and Lin [13]. In this formalism, the amplitude for a transition from the ground state (u_i) to an excited state ($\omega_{i\pm}$), induced by a time-varying external field $v_+ e^{-i\omega t} + v_- e^{i\omega t}$, is given by

$$T = \sum_{i=1}^{N} \int d^3r (\omega_{i+}^{\dagger} \vec{\alpha} \cdot \vec{A} u_i + u_i^{\dagger} \vec{\alpha} \cdot \vec{A} \omega_{i-}). \tag{2}$$

Here the electromagnetic interaction is written in Coulomb gauge and expressed in terms of the Pauli spin matrices $\vec{\alpha} = \begin{pmatrix} 0 & \vec{\sigma} \\ \vec{\sigma} & 0 \end{pmatrix}$ and the vector potential $\vec{A}$.

In a single active electron approximation, the multipole transition amplitude is reduced to

$$T_{JM}^{(\lambda)} = \int d^3r \omega_{i+}^{\dagger} \vec{\alpha} \cdot \vec{a}_{JM}^{\lambda} u_i, \tag{3}$$

where the indices J and M are the photon angular momentum and its projection and $\lambda = 1$ or 0 for electric or magnetic multipoles, respectively. Specifically, for a one-electron transition from an initial state characterized by the quantum numbers ljm to a final continuum state $\bar{l}\bar{j}\bar{m}$ with the spin described by a two-component spinor χ_ν, this equation becomes

$$\begin{aligned} T_{JM}^{(\lambda)} = {} & i\sqrt{\frac{2\pi^2}{Ep}}\sqrt{\frac{(2J+1)(J+1)}{J}}\frac{\omega^J}{(2J+1)!!} \\ & \times \sum_{\bar{\kappa}\bar{m}} [\chi_\nu^{\dagger} \Omega_{\bar{\kappa}\bar{m}}(\hat{p})](-1)^{\bar{j}-\bar{m}} \begin{pmatrix} \bar{j} & J & j \\ -\bar{m} & M & m \end{pmatrix} \\ & \times i^{1-\bar{l}} e^{i\delta_{\bar{\kappa}}} \langle \bar{a} \| Q_J^{(\lambda)} \| a \rangle (-1)^{\bar{j}+j+J}. \end{aligned} \tag{4}$$

Here E and $\hat{p}$ are the photoelectron energy and momentum direction, respectively, ω is the photon frequency, and $\delta_{\bar{\kappa}}$ is the phase of the continuum wave with $\bar{\kappa} = \mp(\bar{j} + \frac{1}{2})$ for $\bar{j} = (\bar{l} \pm \frac{1}{2})$. The spherical spinor is defined as

$$\Omega_{\kappa m}(\hat{n}) = \sum_{\nu=\pm 1/2} C_{l,M-\nu,1/2\nu}^{jM} Y_{lm-\nu}(\hat{n}) \chi_\nu. \tag{5}$$

The corresponding Clebsch-Gordan coefficients are tabulated in Ref. [14]. The reduced matrix element of the spherical tensor between the initial sate $a = (n\kappa)$ and a final energy scale normalized state $a = (E,\bar{\kappa})$ is written as

$$\begin{aligned} \langle \bar{a} \| Q_J^{(\lambda)} \| a \rangle = {} & (-1)^{j+1/2} [\bar{j}][j] \begin{pmatrix} j & \bar{j} & J \\ -1/2 & 1/2 & 0 \end{pmatrix} \\ & \times \pi(\bar{l},l,J-\lambda+1) R_J^{(\lambda)}(\bar{a},a). \end{aligned} \tag{6}$$

Here $\pi(\bar{l},l,J-\lambda+1) = 1$ or 0 for $\bar{l} + l + J - \lambda + 1$ even or odd, respectively, and $R_J^{(\lambda)}(\bar{a},a)$ is the radial integral. While Eq. (6) is derived for a single-electron transition, it also applies to closed-shell atomic systems. In order to include the RRPA correlations, the only change in Eq. (4) is to replace $\langle \bar{a} \| Q_J^{(\lambda)} \| a \rangle$ with $\langle \bar{a} \| Q_J^{(\lambda)} \| a \rangle_{\mathrm{RRPA}}$. Finally, as we will be dealing with electric dipole photoionizing transitions, we set $\lambda = 1$, $J = 1$ and choose $M = 0$, which corresponds to linear polarization in the z direction. In this case, Eq. (4) is reduced to

$$\begin{aligned} T_{10}^{1\pm} \equiv \big[T_{10}^{(1)}\big]_{\nu=\pm 1/2} = {} & \sum_{\bar{\kappa}\bar{m}} C_{l,M-\nu,1/2\nu}^{jM} Y_{lm-\nu}(\hat{p}) \\ & \times \chi_\nu (-1)^{\bar{j}+j+1+\bar{j}-\bar{m}} \begin{pmatrix} \bar{j} & 1 & j \\ -\bar{m} & 0 & m \end{pmatrix} \\ & \times i^{1-\bar{l}} e^{i\delta_{\bar{\kappa}}} \langle \bar{a} \| Q_1^{(1)} \| a \rangle. \end{aligned} \tag{7}$$

Here we dropped the common scaling factor for brevity of notation. We will also be using a shorthand for a reduced matrix element modified by the phase factors:

$$D_{lj\to\bar{l}\bar{j}} = i^{1-\bar{l}} e^{i\delta_{\bar{\kappa}}} \langle \bar{a} \| Q_J^{(\lambda)} \| a \rangle. \tag{8}$$

We note that Eq. (4) differs by the extra parity factor $(-1)^{\bar{j}+j+J}$ from the original equation (43) of Johnson and Lin [13]. We added this factor to make it comply with the Wigner-Eckart theorem [Eq. (107-6) of Landau and Lifshitz [15]].

B. Formulation of angular-dependent time delay

An electric dipole transition from a np initial state leads to the following five ionization channels:

$$\begin{aligned} np_{1/2} &\to \epsilon s_{1/2},\ \epsilon d_{3/2}, \\ np_{3/2} &\to \epsilon s_{1/2},\ \epsilon d_{3/2},\ \epsilon d_{5/2}. \end{aligned}$$

Using Eq. (7), we derive the following expressions for the $np_{1/2}$ ionization amplitude:

$$\begin{aligned} \big[T_{10}^{1+}\big]_{np_{1/2}}^{m=\frac{1}{2}} &= +\frac{1}{\sqrt{15}} Y_{20} D_{np_{1/2}\to\epsilon d_{3/2}} + \frac{1}{\sqrt{6}} Y_{00} D_{np_{1/2}\to\epsilon s_{1/2}}, \\ \big[T_{10}^{1-}\big]_{np_{1/2}}^{m=\frac{1}{2}} &= -\frac{1}{\sqrt{10}} Y_{21}\ D_{np_{1/2}\to\epsilon d_{3/2}}. \end{aligned}$$

Here and throughout the text, $Y_{l,m} \equiv Y_{lm}(\hat{p})$. The corresponding amplitudes with the $m = -1/2$ projection will have a similar structure with the simultaneous inversion of the spin projection $T^+ \leftrightarrow T^-$ and the second index of the spherical harmonic $Y_{21} \to Y_{2-1}$. Each amplitude has its own associated photoelectron group delay (the Wigner time delay [8]) defined as

$$\tau = \frac{d\eta}{dE}\,, \quad \eta = \tan^{-1}\left[\frac{\mathrm{Im} T_{10}^{1\pm}}{\mathrm{Re} T_{10}^{1\pm}}\right]. \tag{9}$$

The spin-averaged time delay can be expressed as a weighted sum:

$$\bar{\tau}_{np_{1/2}} = \frac{\tau_{np_{1/2}}^{m=\frac{1}{2},+} \big|\big[T_{10}^{1+}\big]_{np_{1/2}}^{m=\frac{1}{2}}\big|^2 + \big|\big[T_{10}^{1-}\big]_{np_{1/2}}^{m=\frac{1}{2}}\big|^2 \tau_{np_{1/2}}^{m=\frac{1}{2},-}}{\big|\big[T_{10}^{1+}\big]_{np_{1/2}}^{m=\frac{1}{2}}\big|^2 + \big|\big[T_{10}^{1-}\big]_{np_{1/2}}^{m=\frac{1}{2}}\big|^2}. \tag{10}$$

The angular resolved amplitudes for the $np_{3/2}$ initial state take the following form:

$$\begin{aligned}
\left[T_{10}^{1+}\right]_{np_{3/2}}^{m=1/2} &= \frac{1}{\sqrt{6}}Y_{00}D_{np_{3/2}\to\epsilon s_{1/2}} - \frac{1}{5\sqrt{6}}Y_{20}D_{np_{3/2}\to\epsilon d_{3/2}} \\
&\quad - \frac{1}{5}\sqrt{\frac{3}{2}}Y_{20}D_{np_{3/2}\to\epsilon d_{5/2}}, \\
\left[T_{10}^{1-}\right]_{np_{3/2}}^{m=1/2} &= \frac{1}{10}Y_{21}D_{np_{3/2}\to\epsilon d_{3/2}} - \frac{1}{5}Y_{21}D_{np_{3/2}\to\epsilon d_{5/2}}, \\
\left[T_{10}^{1+}\right]_{np_{3/2}}^{m=3/2} &= -\frac{\sqrt{3}}{10}Y_{21}D_{np_{3/2}\to\epsilon d_{3/2}} - \frac{2\sqrt{3}}{15}Y_{21}D_{np_{3/2}\to\epsilon d_{5/2}}, \\
\left[T_{10}^{1-}\right]_{np_{3/2}}^{m=3/2} &= \frac{\sqrt{3}}{5}Y_{22}D_{np_{3/2}\to\epsilon d_{3/2}} - \frac{\sqrt{3}}{15}Y_{22}D_{np_{3/2}\to\epsilon d_{5/2}}.
\end{aligned}$$

The corresponding spin-averaged time delay becomes

$$\begin{aligned}
\mathcal{S}\,\bar{\tau}_{np_{3/2}} &= \tau_{np_{3/2}}^{m=\frac{1}{2},+}\left|\left[T_{10}^{1+}\right]_{np_{3/2}}^{m=\frac{1}{2}}\right|^2 + \tau_{np_{3/2}}^{m=\frac{1}{2},-}\left|\left[T_{10}^{1-}\right]_{np_{3/2}}^{m=\frac{1}{2}}\right|^2 \\
&\quad + \tau_{np_{3/2}}^{m=\frac{3}{2},+}\left|\left[T_{10}^{1+}\right]_{np_{3/2}}^{m=\frac{3}{2}}\right|^2 + \tau_{np_{3/2}}^{m=\frac{3}{2},-}\left|\left[T_{10}^{1-}\right]_{np_{3/2}}^{m=\frac{3}{2}}\right|^2 \\
\text{with}\quad \mathcal{S} &= \left|\left[T_{10}^{1+}\right]_{np_{3/2}}^{m=\frac{1}{2}}\right|^2 + \left|\left[T_{10}^{1-}\right]_{np_{3/2}}^{m=\frac{1}{2}}\right|^2 \\
&\quad + \left|\left[T_{10}^{1+}\right]_{np_{3/2}}^{m=\frac{3}{2}}\right|^2 + \left|\left[T_{10}^{1-}\right]_{np_{3/2}}^{m=\frac{3}{2}}\right|^2.
\end{aligned}$$

Here we restricted ourselves to positive $m = 1/2,3/2$. The corresponding time delay with negative m will be identical.

C. Nonrelativistic limit

Using Eqs. (6) and (8), we can express the amplitudes via the corresponding radial integrals modified by the phase factors. For a mildly relativistic atom, the radial integrals with $\bar{j} = \bar{l} \pm 1/2$ orbitals will be very similar. Hence we can neglect this difference and reduce the amplitudes to the following expressions:

$$\begin{aligned}
T_{10}^{1+}(np_{1/2}) &= -\frac{1}{3}Y_{00}R_{np\to\epsilon s} - \frac{2}{3}\frac{1}{\sqrt{5}}Y_{20}R_{np\to\epsilon d}, \\
T_{10}^{1+}(np_{3/2}) &= \frac{\sqrt{2}}{3}Y_{00}R_{np\to\epsilon s} + \frac{2}{3}\sqrt{\frac{2}{5}}Y_{20}R_{\epsilon d}, \\
T_{10}^{1-}(np_{1/2}) &= \sqrt{\frac{2}{15}}Y_{21}R_{np\to\epsilon d}, \\
T_{10}^{1-}(np_{3/2}) &= \sqrt{\frac{1}{15}}Y_{21}R_{np\to\epsilon d}.
\end{aligned}$$

This is to be compared with the corresponding nonrelativistic amplitudes [16]:

$$\begin{aligned}
T_{np_{m=0}\to\epsilon s} &= \frac{1}{\sqrt{3}}\;Y_{00}(\hat{n})\;R_{np\to\epsilon s}, \\
T_{np_{m=0}\to\epsilon d} &= 2\sqrt{\frac{1}{15}}\;Y_{20}(\hat{n})\;R_{np\to\epsilon d}, \\
T_{np_{m=1}\to E d} &= -\sqrt{\frac{1}{5}}\;Y_{21}(\hat{n})\;R_{np\to E d}.
\end{aligned}$$

By comparing the weakly relativistic and strictly nonrelativistic amplitudes, we can observe the following scaling properties:

$$\begin{aligned}
&[T^{+}]_{np_{1/2}}^{m=1/2} \simeq \frac{1}{\sqrt{3}}T_{np_{m=0}}, \quad [T^{-}]_{np_{1/2}}^{m=1/2} \simeq -\sqrt{\frac{2}{3}}T_{np_{m=1}}, \\
&[T^{+}]_{np_{3/2}}^{m=1/2} \simeq \sqrt{\frac{2}{3}}T_{np_{m=0}}, \quad [T^{-}]_{np_{3/2}}^{m=1/2} \simeq -\frac{1}{\sqrt{3}}T_{np_{m=1}}, \\
&[T^{+}]_{np_{3/2}}^{m=3/2} \simeq T_{np_{m=1}}, \quad [T^{-}]_{np_{3/2}}^{m=3/2} \simeq 0.
\end{aligned} \tag{11}$$

By feeding this scaling into the spin-averaged time delay expressions, we get

$$\bar{\tau}_{np_{1/2}} = \frac{\tau_{np_{m=0}}|T_{np_{m=0}}|^2 + 2\tau_{np_{m=1}}|T_{np_{m=1}}|^2}{|T_{np_{m=0}}|^2 + 2|T_{np_{m=1}}|^2} \simeq \bar{\tau}_{np},$$

which represents the magnetic projection average nonrelativistic time delay as used in Ref. [4]. By the same token,

$$\bar{\tau}_{np_{3/2}} = \frac{2\tau_{np_{m=0}}|T_{np_{m=0}}|^2 + 4\tau_{np_{m=1}}|T_{np_{m=1}}|^2}{2|T_{np_{m=0}}|^2 + 4|T_{np_{m=1}}|^2} \simeq \bar{\tau}_{np}.$$

D. Angular anisotropy parameters

As an additional test, we plugged the reduced matrix elements (8) into expressions for the angular anisotropy β parameters [17]:

$$\begin{aligned}
\beta_{np_{1/2}} &= \frac{|D_{d_{3/2}}|^2 - 2\sqrt{2}\mathrm{Re}[D_{d_{3/2}}^{*}D_{s_{1/2}}]}{|D_{d_{3/2}}|^2 + |D_{s_{1/2}}|^2}, \\
\mathcal{S}\beta_{np_{3/2}} &= 4|D_{d_{5/2}}|^2 - 4|D_{d_{3/2}}|^2 + 6\mathrm{Re}[\tilde{D}_{d_{5/2}}^{*}\tilde{D}_{d_{3/2}}] \\
&\quad - 2\sqrt{5}\mathrm{Re}[\tilde{D}_{d_{3/2}}^{*}\tilde{D}_{s_{1/2}}] - 6\sqrt{5}\mathrm{Re}[\tilde{D}_{d_{5/2}}^{*}\tilde{D}_{s_{1/2}}], \\
\text{with}\quad \mathcal{S} &= 5(|D_{d_{5/2}}|^2 + |D_{d_{3/2}}|^2 + |D_{s_{1/2}}|^2),
\end{aligned} \tag{12}$$

which both should converge, in a weakly relativistic limit, to the nonrelativistic expression [18]

$$\beta_{np} = \frac{\{3|D_d|^2 + 6\sqrt{2}\mathrm{Re}(D_d^{*}D_s)\}}{3\{|D_d|^2 + |D_s|^2\}}. \tag{13}$$

This test is indeed satisfied.

III. RESULTS AND DISCUSSION

The RRPA calculations have been performed with the following channels coupled: 14 channels for Ar (all dipole excitations from the $3p$, $3s$, and $2p$ subshells), 18 channels for Kr (excitations from the $4p$, $4s$, $3d$, and $3p$ subshells), and 18 channels for Xe (the $5p$, $5s$, $4d$, and $4p$ subshells). In addition, where available, experimental threshold energies from Ref. [19] were used to facilitate better comparison with experiment. These energies are identical to those displayed in Table 1 of Ref. [11].

A. Argon

Argon is hardly a relativistic target and chosen here only for validation and calibration of our theoretical model against the previous calculations [4,5] and experiment [21]. It is also used to test numerical compatibility of the RRPA code with the nonrelativistic RPAE code used in previous time delay calculations [16].

Results of the Ar calculations in the photon energy range encompassing the Cooper minimum are summarized in Fig. 1. On the top panel we show the angular anisotropy β parameters calculated by the RRPA and RPAE codes using the relativistic (12) and nonrelativistic (13) expressions, respectively. A slight displacement of the very close relativistic curves for $\beta_{3p_{1/2}}$ and $\beta_{3p_{3/2}}$ with respect to the nonrelativistic result β_{3p} can be seen near the Cooper minimum. The experimental data [20] agree well with both the RRPA and RPAE calculations, with a sight tendency towards the RRPA. However, the error bars are too large to discriminate between the two models. Given the fact that the $\beta_{3p_{1/2}}$ and $\beta_{3p_{3/2}}$ curves are hardly distinguishable on the scale of the figure, their difference with nonrelativistic β_{3p} is more indicative of the numerical compatibility of the two codes rather than true relativistic effects.

The Wigner time delay τ_W of Ar $3p_{1/2}$ and $3p_{3/2}$ subshells is shown in Fig. 1 for the fixed emission angles $\theta = 0^\circ$ (the second top panel) and $\theta = 45^\circ$ (the third panel). Comparison is made with the two nonrelativistic RPAE calculations [16] and [4] (marked as RPAE and RPAE-2, respectively) and the third RPAE calculation augmented by the exterior complex scaling (ECS-RPAE) to implement boundary conditions [5]. The latter calculation returned the total atomic time delay (1) and contained the CLC component, whereas neither the present RRPA results nor the literature RPAE results [4,16] were corrected for CLC. The bottom panel displays the angular-averaged results from different calculations and a comparison with a RABBITT experiment [21] in which no discrimination with the photoelectron direction was made.

In the polarization direction at $\theta = 0^\circ$, the present RRPA results and nonrelativistic RPAE results [4,16] agree very well. Displacement of the RRPA and RPAE time delays at the bottom of the Cooper minimum is slightly bigger than the corresponding β results on the top panel. The time delay of the $3p_{1/2}$ and $3p_{3/2}$ subshells is very close, indicating that the spin-orbit interaction is not important here. The ECS-RPAE calculation [5] includes both the components of the atomic time delay (1) and hence differs noticeably.

At the fixed photoelectron emission angle $\theta = 45^\circ$, the RPAE results [4,16] and the present RRPA calculation are still rather close. However, the ECS-RPAE calculations is considerably further away than in the case of $\theta = 0^\circ$. In a private communication, Dahlström [22] explains this deviation by the following consideration. The ϵd continuum is converted to the p and f waves by the IR photon absorption in two-color photoionization experiments. The f wave passes through a kinematic node close to 45° and hence diminishes the effective contribution of the d wave to the Wigner time delay. Hence the energy dependence of the time delay near the Cooper minimum becomes less pronounced. When the angular average is taken (bottom panel), the difference between all the calculations is not so pronounced, and they compare reasonably well with the experiment [21]. A more accurate angular-resolved measurement is needed to validate various theoretical predictions in the directions away from the polarization axis.

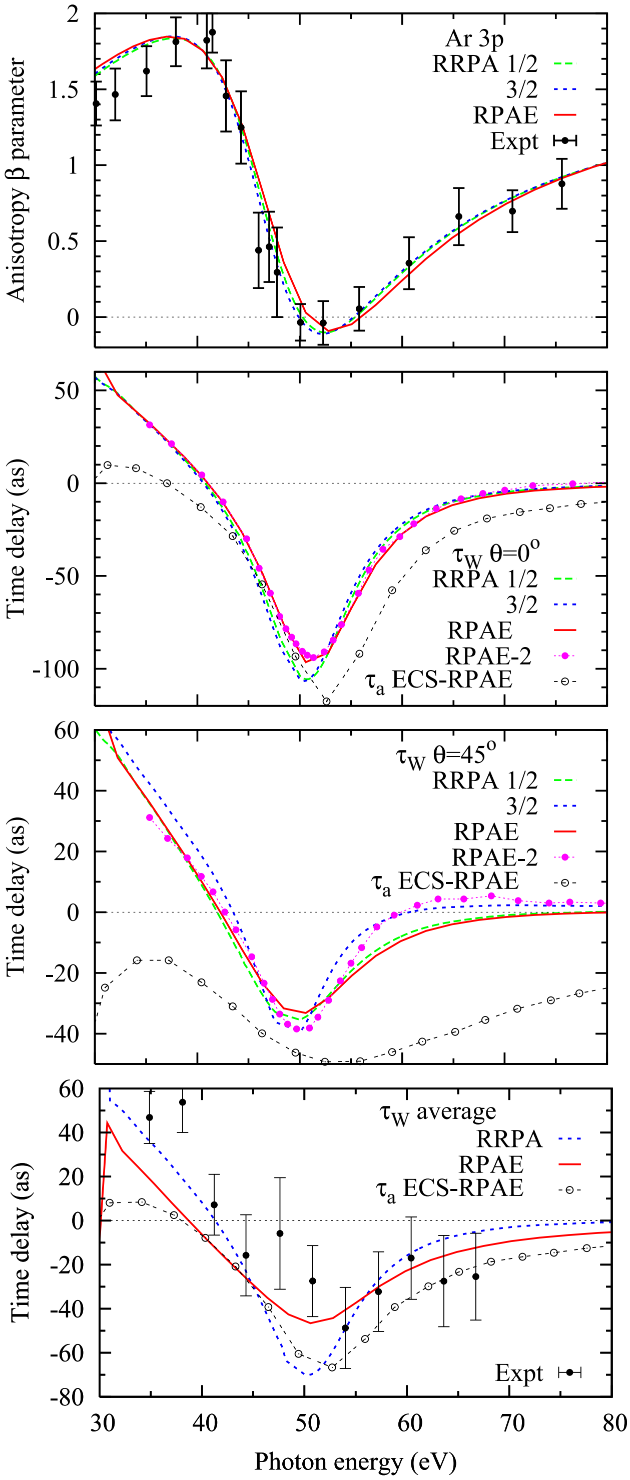

FIG. 1. Top: The angular anisotropy parameters $\beta_{3p_{1/2}}$ (green dashed line) and $\beta_{3p_{3/2}}$ (blue dotted line) from the RRPA calculation and β_{3p} from the RPAE calculation (red solid line). The experiment (error bars) is from Ref. [20]. Other panels: The Wigner time delay τ_W of Ar $3p_{1/2}$ and $3p_{3/2}$ (same line styles). The nonrelativistic RPAE results from Ref. [16] and RPAE-2 from Ref. [4] are shown by the red solid line and red filled circles, respectively. The total atomic time delay τ_a from the ECS-RPA calculation of Ref. [5] is plotted with open circles. The second top panel: $\theta = 0^\circ$, third panel: $\theta = 45^\circ$, bottom panel: angular average. The experimental data from Ref. [21] are shown on the bottom panel with error bars.

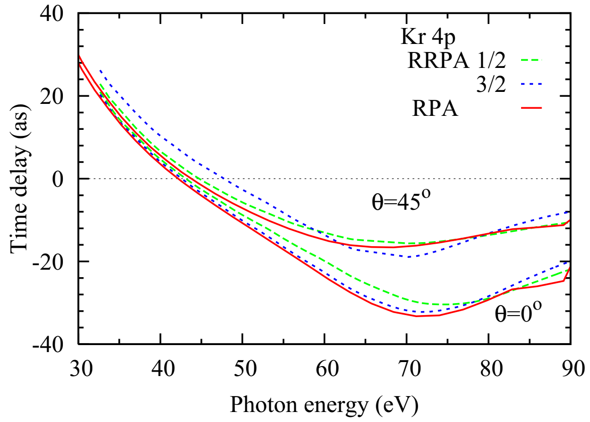

FIG. 2. The time delay of Kr $4p_{1/2}$ (green dashed line) and $4p_{3/2}$ (blue dotted line) is plotted versus the photon energy in the fixed emission directions $\theta = 0^\circ$ and $\theta = 45^\circ$. The nonrelativistic RPAE result from Ref. [16] is shown by the red solid line. The angular-averaged experimental data from Ref. [21] are shown with error bars.

B. Krypton and xenon

The time delay of Kr $4p_{1/2}$ and $4p_{3/2}$ subshells in the energy range encompassing the Cooper minimum is shown in Fig. 2 in the two fixed directions $\theta = 0^\circ$ and $\theta = 45^\circ$. The time delay displays the characteristic dip near the Cooper minimum but not as deep as in the case of argon. The depth of the minimum indicates the relative strength of the nominally weaker channel near the Cooper minimum of the normally stronger channel. In the nonrelativistic RPAE model, this stronger channel can be identified with the $4p_{m=0} \to \epsilon d$ transition. Other angular momentum projections $m = \pm 1$ in this channel are excluded in the $\theta = 0^\circ$ polarization direction. Away from this direction, weaker channels $4p_{m=\pm 1} \to \epsilon d$, along with the $4p_{m=0} \to \epsilon s$ channel, also make their contribution to the photoionization amplitude and the time delay. Hence the Cooper minimum in the time delay is getting shallower. Overall the angular dependence is much weaker in Kr than in the case of Ar. Nevertheless, the RRPA calculations show a noticeable deviation from the RPAE, and the spin-orbit splitting of the time delay becomes visible.

The analogous set of data for the Xe $5p_{1/2}$ and $5p_{3/2}$ subshells is shown in Fig. 3. The photon energy range near the Cooper minimum encompasses two series of autoionization resonances $5s^1np$ [23] and $4d^9np$ [24]. These resonances cause rapid oscillations of the time delay, which are well resolved in the present RRPA calculation but not so well in the RPAE [16]. As in the case of Kr, the relativistic effects are noticeable in Xe. Similar to other atoms, the Cooper minimum of the time delay is flattening away from the polarization direction.

C. Near-threshold region

The time delay near the threshold is dominated strongly by the Coulomb singularity. The scattering phase of the photoelectron propagating in the field of the singly charged parent ion diverges to negative infinity as the photoelectron energy goes to zero [25]. Correspondingly, the photoelectron group delay (the Wigner time delay) tends to positive infinity near threshold. The CLC correction has a similar logarithmic singularity [10], but it is negative. So the total atomic time delay (1) is the sum of the two divergent terms of the opposite signs.

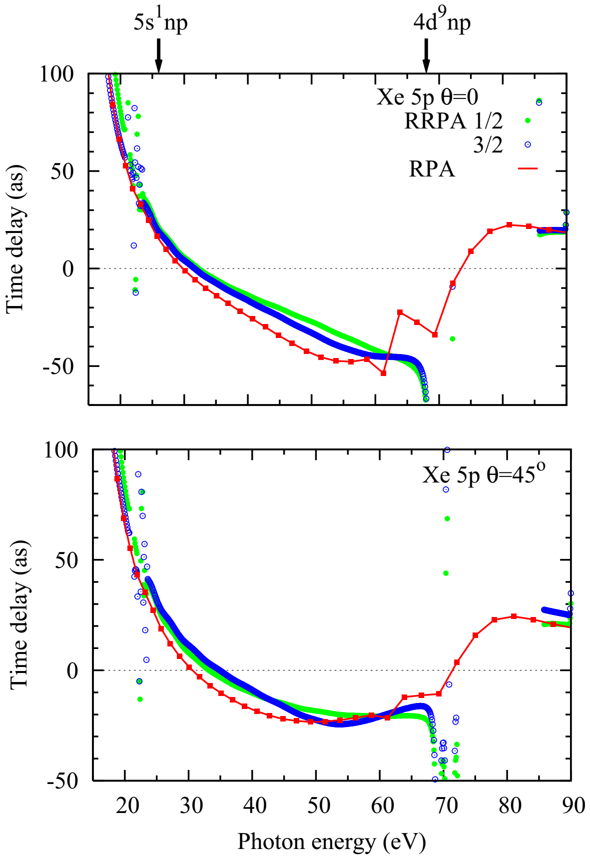

FIG. 3. The time delay of Xe $5p_{1/2}$ (green filled circles) and $5p_{3/2}$ (blue open circles) is plotted versus the photon energy. The nonrelativistic RPAE result from Ref. [16] is shown by the red solid line. Regions of the autoionization series $5s^1np$ [23] and $4d^9\,np$ [24] are marked by vertical arrows.

In the near-threshold experiment [7], it is the difference of the atomic time delays in the $np_{1/2}$ and $np_{3/2}$ subshells that is measured. Because of the different ionization potentials, the photoelectron ejected from the deeper $np_{1/2}$ subshell has a smaller kinetic energy than the one ionized from the $np_{3/2}$ subshell. Hence the Wigner time delay in the $np_{1/2}$ subshell is larger than the $np_{3/2}$ subshell at the same photon energy. This characteristic behavior is seen on the top panels of Fig. 4 for Kr and Fig. 5 for Xe. The same difference in the photoelectron kinetic energies will affect the respective CLC corrections to the time delay in the $np_{1/2}$ and $np_{3/2}$ subshells. To account for this effect, we used the values of $\tau_{\rm CLC}$ plotted in Fig. 5 of Ref. [10] as a function of the photoelectron energy. We fitted it with an analytical formula and calculated the difference $\tau^{3/2}_{\rm CLC} - \tau^{1/2}_{\rm CLC}$ due to the difference in respective ionization potentials. The corresponding difference for the Wigner time delay $\tau^{3/2}_{\rm W} - \tau^{1/2}_{\rm W}$ was extracted from the RRPA calculations. The area of the autoionization resonances was excluded from this procedure because of the rapid variation of the Wigner time delay in this region.

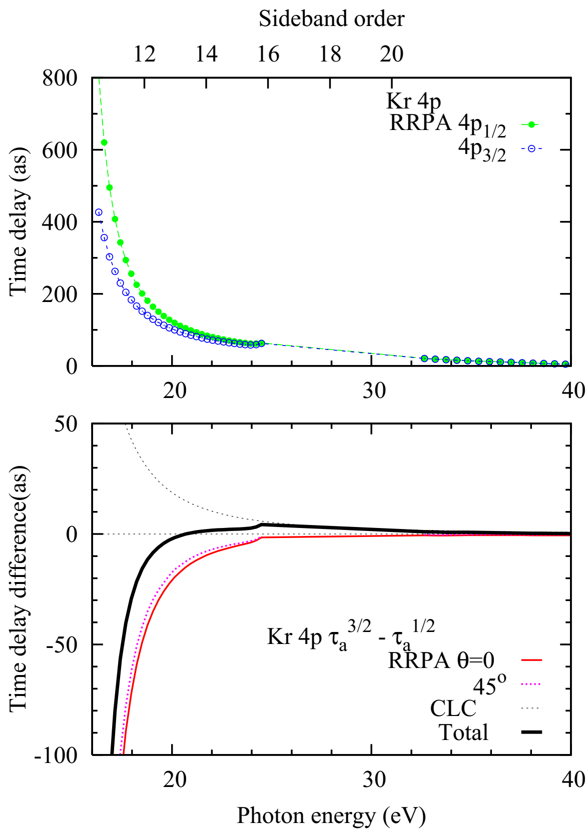

FIG. 4. The atomic time delay in the Kr $4p$ subshell. Top: The Wigner time delay from the $4p_{1/2}$ and $4p_{3/2}$ subshells is shown with filled green circles and open blue circles, respectively. Bottom: The time delay difference $\tau_a^{3/2} - \tau_a^{1/2}$. The raw RRPA calculations at $\theta = 0^\circ$ and 45° are shown with the red solid and purple dashed lines, respectively. The CLC correction from Ref. [10] is visualized with a thin dotted line. The RRPA result at $\theta = 0^\circ$ corrected by the CLC is shown with a thick solid line.

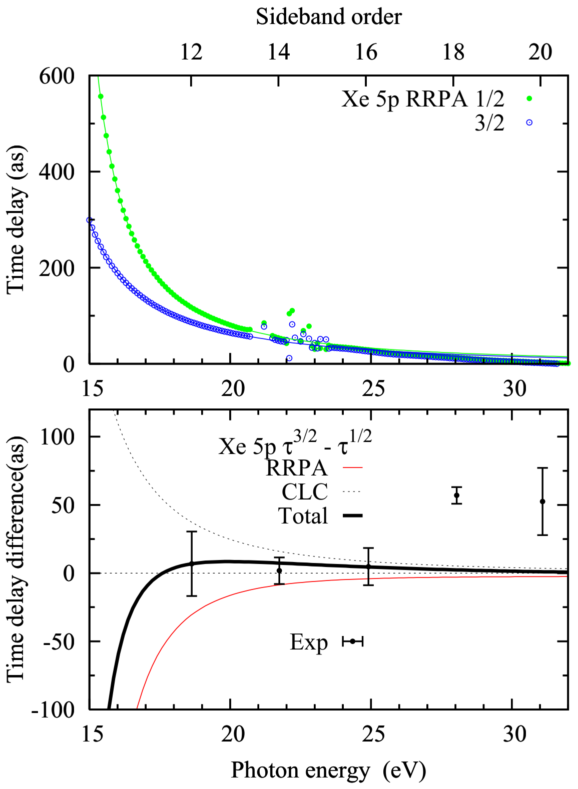

FIG. 5. Same as Fig. 4 for Xe $5p$ subshell. The experimental data from Ref. [7] are plotted with error bars.

The resulting values of the time delay difference are shown in the bottom panels of Fig. 4 and Fig. 5 for Kr and Xe, respectively. In the case of Kr, the angular dependence of the time delay difference $\tau_{\mathrm{W}}^{3/2} - \tau_{\mathrm{W}}^{1/2}$ is small as can be seen in comparison of the values obtained for the two fixed scattering angles $\theta = 0^\circ$ and $\theta = 45^\circ$. Hence the values of the atomic time delay difference $\tau_a^{3/2} - \tau_a^{1/2}$ evaluated in the direction of the polarization axis can be compared with the angular-averaged experiment [7]. In the case of Xe, this difference is even smaller and not noticeable in the scale of the bottom panel of Fig. 5.

In comparison to Kr, Xe has smaller ionization thresholds. Hence, at the same photon energy, the photoelectrons have larger kinetic energy, which takes them farther away from the threshold. Therefore, the effect of the Coulomb singularity on the Wigner time delay and the CLC correction is weaker. The net atomic time delay difference in Xe becomes positive near threshold, whereas it is negative or close to zero in the case of Kr. These findings are in line with the experiment [7] except of the two points at higher photon energy. This difference persists in a new set of experimental data [26].

IV. CONCLUSIONS

We applied the relativistic formalism and RRPA computational scheme to evaluate the time delay in the valence shell of noble gas atoms, Ar, Kr, and Xe. The two characteristic features of the time delay are analyzed: the angular dependence near the Cooper minimum and the effect of the spin-orbit splitting near the threshold. Comparison with nonrelativistic calculations serves as a convenient test and a calibration tool. The effect of the spin-orbit splitting is not strong near the Cooper minimum, which is relatively far from the ionization threshold. However, the angular dependence is significant in this photon energy range due to efficient competition of the nominally weak and strong photoionization channels. This dependence is most pronounced in Ar. Indirectly, this angular dependence is confirmed by the angular integrated experiment [21], which agrees much better with angular-averaged calculations rather than angular specific data. In heavier noble gases, Kr and Xe, the angular dependence is also noticeable but not as pronounced as in Ar.

The time delay in the near-threshold region shows little or no angular dependence while the spin-orbit splitting effect is large. At the same photon energy, the photoelectron ejected from a deeper $np_{1/2}$ subshell has smaller kinetic energy and is less affected by the Coulomb singularity as its counterpart ejected from the shallower $np_{3/2}$ subshell. The corresponding difference in the Wigner time delays is offset by the difference in the correction due to the Coulomb-laser coupling. As a result, the net atomic delay difference becomes positive in Xe and remains negative in Kr. These findings are in line with recent experimental observations [7].

ACKNOWLEDGMENTS

The authors wish to thank Hans Jakob Wörner for many stimulating discussions and Marcus Dahlström for useful comments. A.S.K. acknowledges the support of the ARC Discovery grant DP120101805. A.M. thanks Dr. G. Aravind, Department of Physics, IIT Madras, India, for very fruitful discussions. V.K.D. acknowledges the support of the NSF under Grant No. PHY-1305085. P.C.D. acknowledges the support of a grant from the Department of Science and Technology, Government of India. S.T.M. was supported by the Division of Chemical Sciences, Basic Energy Science, Office of Science, US Department of Energy.

---

[1] M. Schultze *et al.*, Delay in photoemission, Science **328**, 1658 (2010).

[2] K. Klünder, J. M. Dahlström, M. Gisselbrecht, T. Fordell, M. Swoboda, D. Guénot, P. Johnsson, J. Caillat, J. Mauritsson, A. Maquet *et al.*, Probing Single-Photon Ionization on the Attosecond Time Scale, Phys. Rev. Lett. **106**, 143002 (2011).

[3] R. Pazourek, S. Nagele, and J. Burgdörfer, Attosecond chronoscopy of photoemission, Rev. Mod. Phys. **87**, 765 (2015).

[4] J. Wätzel, A. S. Moskalenko, Y. Pavlyukh, and J. Berakdar, Angular resolved time delay in photoemission, J. Phys. B **48**, 025602 (2015).

[5] J. M. Dahlström and E. Lindroth, Study of attosecond delays using perturbation diagrams and exterior complex scaling, J. Phys. B **47**, 124012 (2014).

[6] S. Heuser, Á. Jiménez Galán, C. Cirelli, M. Sabbar, R. Boge, M. Lucchini, L. Gallmann, I. Ivanov, A. S. Kheifets, J. M. Dahlström *et al.*, Time delay anisotropy in photoelectron emission from the isotropic ground state of helium, J. Phys.: Conf. Ser. **635**, 092089 (2015).

[7] M. Huppert, I. Jordan, S. Pabst, and H. J. Wörner, Relativistic photoionization delays and the role of auto-ionizing resonances, J. Phys.: Conf. Ser. **635**, 092135 (2015).

[8] E. P. Wigner, Lower limit for the energy derivative of the scattering phase shift, Phys. Rev. **98**, 145 (1955).

[9] R. Pazourek, S. Nagele, and J. Burgdorfer, Time-resolved photoemission on the attosecond scale: opportunities and challenges, Faraday Discuss. **163**, 353 (2013).

[10] J. Dahlström, D. Guénot, K. Klünder, M. Gisselbrecht, J. Mauritsson, A. L. Huillier, A. Maquet, and R. Taïeb, Theory of attosecond delays in laser-assisted photoionization, Chem. Phys. **414**, 53 (2012).

[11] S. Saha, A. Mandal, J. Jose, H. R. Varma, P. C. Deshmukh, A. S. Kheifets, V. K. Dolmatov, and S. T. Manson, Relativistic effects in photoionization time delay near the Cooper minimum of noble-gas atoms, Phys. Rev. A **90**, 053406 (2014).

[12] A. S. Kheifets, S. Saha, P. C. Deshmukh, D. A. Keating, and S. T. Manson, Dipole phase and photoelectron group delay in inner-shell photoionization, Phys. Rev. A **92**, 063422 (2015).

[13] W. R. Johnson and C. D. Lin, Multichannel relativistic random-phase approximation for the photoionization of atoms, Phys. Rev. A **20**, 964 (1979).

[14] D. A. Varshalovich, A. N. Moskalev, and V. K. Khersonskii, *Quantum Theory of Angular Momentum* (World Scientific, Philadelphia, 1988).

[15] L. D. Landau and E. M. Lifshitz, *Quantum Mechanics (Non-relativistic theory)*, Vol. 3 of Course of Theoretical Physics, 3rd ed. (Pergamon Press, Oxford, 1985).

[16] A. S. Kheifets, Time delay in valence-shell photoionization of noble-gas atoms, Phys. Rev. A **87**, 063404 (2013).

[17] U. Heinzmann, Experimental determination of the phase differences of continuum wavefunctions describing the photoionisation process of xenon atoms. I. Measurements of the spin polarisations of photoelectrons and their comparison with theoretical results, J. Phys. B **13**, 4353 (1980).

[18] M. Y. Amusia, *Atomic Photoeffect* (Plenum Press, New York, 1990).

[19] Y. Ralchenko, A. E. Kramida, J. Reader, and NIST ASD Team, NIST Atomic Spectra Database (version 3.1.5), Tech. Rep., National Institute of Standards and Technology, Gaithersburg, MD (2011), http://physics.nist.gov/asd.

[20] R. G. Houlgate, K. Codling, G. V. Marr, and J. B. West, Angular distribution and photoionization cross section measurements on the 3p and 3s subshells of argon, J. Phys. B **7**, L470 (1974).

[21] C. Palatchi, J. M. Dahlström, A. S. Kheifets, I. A. Ivanov, D. M. Canaday, P. Agostini, and L. F. DiMauro, Atomic delay in helium, neon, argon and krypton, J. Phys. B **47**, 245003 (2014).

[22] J. M. Dahlström (private communication).

[23] K. Codling and R. P. Madden, Resonances in the photoionization continuum of Kr and Xe, Phys. Rev. A **4**, 2261 (1971).

[24] D. L. Ederer and M. Manalis, Photoabsorption of the 4d electrons in xenon, J. Opt. Soc. Am. **65**, 634 (1975).

[25] J. C. A. Barata, L. F. Canto, and M. S. Hussein, New asymptotic formulas for the point Coulomb phase shift, Braz. J. Phys. **41**, 50 (2011).

[26] I. Jordan, M. Huppert, S. Pabst, A. S. Kheifets, D. Baykusheva, and H. J. Wörner, Relativistic delays in photoemission: A precision test for experiment and theory (unpublished).